

# Nanoscale

Accepted Manuscript



This is an *Accepted Manuscript*, which has been through the Royal Society of Chemistry peer review process and has been accepted for publication.

*Accepted Manuscripts* are published online shortly after acceptance, before technical editing, formatting and proof reading. Using this free service, authors can make their results available to the community, in citable form, before we publish the edited article. We will replace this *Accepted Manuscript* with the edited and formatted *Advance Article* as soon as it is available.

You can find more information about *Accepted Manuscripts* in the [Information for Authors](#).

Please note that technical editing may introduce minor changes to the text and/or graphics, which may alter content. The journal's standard [Terms & Conditions](#) and the [Ethical guidelines](#) still apply. In no event shall the Royal Society of Chemistry be held responsible for any errors or omissions in this *Accepted Manuscript* or any consequences arising from the use of any information it contains.

Cite this: DOI: 10.1039/c0xx00000x

www.rsc.org/xxxxxx

ARTICLE TYPE

# Hybrid Nanostructure of MnCo<sub>2</sub>O<sub>4.5</sub> Nanoneedle/Carbon Aerogel for Symmetric Supercapacitors with High Energy Density

Cite this: DOI: 10.1039/x0xx00000x

Pin Hao<sup>a,b</sup>, Zhenhuan Zhao<sup>a</sup>, Liyi Li<sup>b</sup>, Chia-Chi Tuan<sup>b</sup>, Haidong Li<sup>a</sup>, Yuanhua Sang<sup>a</sup>, Huaidong Jiang<sup>a</sup>, C.P. Wong<sup>b\*</sup>, Hong Liu<sup>a\*</sup>Received xxth xxx 2014,  
Accepted xxth, xxx 2014

DOI: 10.1039/x0xx00000x

www.rsc.org/

Current applications of carbon-based supercapacitors are limited by low energy density. One promising strategy to enhance the energy density is to couple metal oxides with carbon materials. In this study, porous MnCo<sub>2</sub>O<sub>4.5</sub> nanoneedle/carbon aerogel hybrid nanostructure was synthesized by assembling MnCo<sub>2</sub>O<sub>4.5</sub> nanoneedle arrays on the surface of channel walls of hierarchical porous carbon aerogels derived from chitosan for the supercapacitor application. The synthetic process of the hybrid nanostructure involves two steps, *i.e.*, the growth of Mn-Co precursors on carbon aerogel by a hydrothermal process and the conversion of the precursor into MnCo<sub>2</sub>O<sub>4.5</sub> nanoneedles by calcination. The carbon aerogel exhibits high electrical conductivity, high specific surface area and porous structure, ensuring high electrochemical performance of the hybrid nanostructure when coupled with the porous MnCo<sub>2</sub>O<sub>4.5</sub> nanoneedles. The symmetric supercapacitor using MnCo<sub>2</sub>O<sub>4.5</sub> nanoneedle/carbon aerogel hybrid nanostructure as the active electrode material exhibits high energy density of about 84.3 Wh kg<sup>-1</sup> at a power density of 600 W kg<sup>-1</sup>. The voltage window is as high as 1.5 V in neutral aqueous electrolyte. Due to the unique nanostructure in the electrodes, the capacitance retention reaches 86% over 5000 cycles.

## 1. Introduction

Extensive research has been committed to developing renewable energy systems in order to respond to the increasing energy demand and to the need of reducing environmental pollution.<sup>1,2</sup> Supercapacitor has emerged as a promising device for energy storage. Compared to rechargeable lithium-ion batteries, supercapacitors are much safer with higher powder density, longer cycle-life and much shorter charging time. However, low energy density of supercapacitors is still an obstacle for their practical applications as power storage devices.<sup>3</sup> In the past few years, the enhancement of energy density by developing high-quality nanostructured materials has seen a significant progress.<sup>4-6</sup> However, the energy density of supercapacitors is still lower than that of batteries by an order of magnitude. Furthermore, achieving high energy density while maintaining high power density and long cyclability is still a challenge for supercapacitors.<sup>7</sup> It is expected that these demands can be met by innovative design of electrochemically active, nanostructured materials to be used the supercapacitor electrodes.

Taking into account the definition of energy density as the following,

$$E = (CV^2) / 2$$

where  $C$  is the specific capacitance of the electrode and  $V$  is the voltage across the electrode,<sup>8</sup> the energy density of the supercapacitor can be enhanced by two strategies: increasing the

specific capacitance or broadening the voltage window.

The first approach to enhancing the energy density is to increase the specific capacitance. The specific capacitance of a supercapacitor is determined by the materials and the structure of the active electrodes.<sup>9</sup> Carbon materials, including activated carbon, carbon fibers, carbon nanotubes, carbon aerogels, and graphene are commonly used as supercapacitor electrode materials due to their high electrical conductivity, high specific surface area and well-developed microstructure.<sup>10-14</sup> Carbon materials store electric energy through electrical double layer, and the capacitance of which is affected by several parameters, such as the electrical conductivity, specific surface area, pore size and pore size distribution of the carbon materials.<sup>3</sup> The ideal electrode material should have a hierarchical porous structure consisted of macropores (larger than 50 nm) for the ion-buffering reservoir, mesopores (2~50 nm) for ion transportation and micropores (less than 2 nm) for charge storage.<sup>3</sup> It is desirable for the porous carbon structures to have porosity on multiple size-scale.<sup>15, 16</sup> Unfortunately, the enhancement of the specific surface area of carbon materials is still limited, hence the capacitance of carbon materials is only 50~200 F g<sup>-1</sup>, resulting in a low energy density. On the other hand, transition metal oxides such as RuO<sub>2</sub>, MnO<sub>2</sub>, Ni(OH)<sub>2</sub>, Co<sub>2</sub>O<sub>3</sub>, usually have very high theoretical specific capacitance and are widely used for pseudocapacitors which store energy through redox reactions.<sup>17-23</sup> Therefore, coupling metal oxides with carbon materials in the electrode can be a plausible strategy to enhance the specific capacitance.

Recently, many mixed transition metal oxides (MTMOs) with spinel structure have received an upsurge in interest due to their low cost, environmentally friendliness and high performance in many energy storage applications. The coupling of two metal cations could endow the MTMOs with rich redox reaction sites. In addition, the various combinations of cations, and the tunable stoichiometric/non-stoichiometric compositions of the MTMOs allow the manipulation of the physical and/or chemical properties.<sup>24</sup> As one of the ternary MTMOs,  $Mn_xCo_{3-x}O_y$  has been also used for energy storage both in supercapacitors and Li-ion batteries. For example, L. Li *et al.* prepared  $MnCo_2O_4$  nanowire arrays as the electrode materials for supercapacitors and Li-ion batteries. The nanowire array exhibited noticeable electrochemical performance enhancement with a high capacitance of  $349.8 \text{ F g}^{-1}$  at  $1 \text{ A g}^{-1}$  and an initial specific discharge capacity of  $1288.6 \text{ mAh g}^{-1}$  at  $100 \text{ mA g}^{-1}$ .<sup>25</sup> Porous  $MnCo_2O_{4.5}$  nanowires fabricated by W. Li *et al.* exhibited a specific capacitance of  $151.2 \text{ F g}^{-1}$  at  $5 \text{ mV s}^{-1}$ , indicating that  $MnCo_2O_{4.5}$  is a promising electrode material for supercapacitors.<sup>24</sup> Therefore, to grow porous  $MnCo_2O_{4.5}$  nanostructures on porous carbon aerogel could be an effective method to increase the specific capacitance for supercapacitor electrode.

The second approach to increasing the energy density is to broaden the voltage window. The voltage window of a symmetric supercapacitor is determined by the type of electrolyte. It is well accepted that the voltage window of a supercapacitor in aqueous electrolyte, organic electrolyte and ionic liquids is about 1.2 V, 2.7 V and 4.0 V, respectively. However, organic electrolytes usually bring a problem about the decrease of the energy storage performance due to the increased resistance and poor ion transportation compared with aqueous electrolytes.<sup>26, 27</sup> Therefore, supercapacitors using organic electrolytes often show low capacitance and poor power rates. Furthermore, organic electrolyte is toxic and not environmental friendly. Electrolyte depletion upon charge, narrow operational temperature range, and safety issues are three major drawbacks of organic electrolytes.<sup>28</sup> Although ionic liquids offer high ionic conductivity, high electrochemical stability, high energy density, and environmental-friendliness, and can deliver a voltage window of about 4.0 V, the high cost of ionic liquids limits their applications in supercapacitors. On the other hand, aqueous electrolytes are widely applied to supercapacitors because of their lower cost, environment friendliness and ease of use, as well as high conductivity and low viscosity. However, the working voltage in aqueous electrolyte is thermodynamically limited to 1.2 V due to water decomposition at 1.23 V.<sup>29</sup> Therefore, it is challenging to extend the voltage window of supercapacitors in aqueous electrolytes.<sup>29</sup> Depending on the characteristics of the electrode materials,  $H_2SO_4$ , KOH,  $Na_2SO_4$ , and other neutral aqueous solutions are selected as the aqueous electrolytes in supercapacitors.<sup>30-33</sup> Because  $H_2SO_4$  and KOH solutions possess high corrosivity, neutral aqueous solutions are commonly used as the electrolyte for supercapacitor electrodes. In addition, due to the high catalytic activity of metal oxides, the water splitting reaction for hydrogen and oxygen evolution in acidic and alkaline

electrolytes occurs readily while this process can be inhibited because of the weakened polarization in neutral electrolytes. One promising protocol to extend the voltage window of supercapacitors in aqueous electrolytes is to assemble supercapacitors using carbon and metal oxide hybrid nanostructures. In hybrid nanostructures-based supercapacitors, because of the presence of both electrochemical double layer capacitance and pseudocapacitance, the voltage window can typically extend to 1.8 V.<sup>34</sup> Recently, Krzysztof, Fic and coworkers systematically proved the possibility of efficient capacitor working in a wider voltage range of 2.2 V in  $1 \text{ mol L}^{-1}$   $Li_2SO_4$  aqueous electrolyte due to the strong solvation of  $Li^+$  and  $SO_4^{2-}$ .<sup>26</sup>

In this study, we report the synthesis of  $MnCo_2O_{4.5}$  nanoneedles/carbon aerogel composites with a hierarchical porous structure for the application of supercapacitor. To the best of our knowledge, this is the first report about the manganese-based MTMOs-carbon aerogel nanostructured architectures used for supercapacitors. The assembled supercapacitor exhibits high specific capacitance and high energy density, and more impressively, the voltage window is as high as 1.5 V in aqueous electrolyte. The symmetric supercapacitor shows high cyclability and there is no significant capacitance reduction after 5000 cycles.

## 2. Experimental

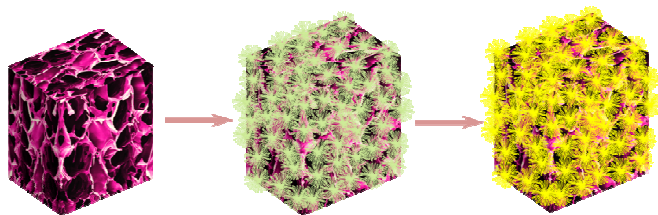
### 2.1 Preparation of hierarchical porous carbon aerogels

Carbon aerogels were synthesized by using chitosan (deacetylation  $\geq 95\%$ , viscosity 100-200 mPa·s, Aladdin) as the raw material through a carefully controlled aerogel formation-carbonization-activation process, as detailed in our previous study.<sup>35</sup> A typical synthesis procedure is as following. 1 g of chitosan powder was dispersed in 40 mL of deionized water followed by the addition of 0.8 mL of acetic acid (Fisher Chemicals) with vigorous stirring until a transparent chitosan solution with high viscosity was obtained. Then, the chitosan solution was frozen to  $-40 \text{ }^\circ\text{C}$  for 24 h and dried using freeze dryer to form chitosan aerogels. The chitosan aerogels were pyrolyzed at  $800 \text{ }^\circ\text{C}$  for 3 h in the Ar atmosphere at the heating rate of  $3 \text{ }^\circ\text{C min}^{-1}$  to prepare carbonized aerogels. The as-prepared carbon aerogels were homogeneously mixed with KOH (Alfa Aesar) solution at the KOH/carbon aerogel weight ratio of 3:1. Then the mixture was dried at  $100 \text{ }^\circ\text{C}$  to remove the water and was further activated at  $700 \text{ }^\circ\text{C}$  at the heating rate of  $5 \text{ }^\circ\text{C min}^{-1}$  and held for 2 h under Ar atmosphere. After activation, the sample was washed deionized water and then dried at  $70 \text{ }^\circ\text{C}$  overnight.

### 2.2 Preparation of 3D $MnCo_2O_{4.5}$ nanoneedles/carbon aerogel hybrid nanostructure

The hierarchical porous carbon aerogel described above was used as the substrate for the growth of  $MnCo_2O_{4.5}$  nanoneedle arrays. In a typical synthesis, an 80 mL aqueous solution containing 0.002 mol of  $Co(NO_3)_2$  (Alfa Aesar), 0.001 mol of  $Mn(NO_3)_2$  (Alfa Aesar), 0.012 mol of urea (Alfa Aesar) was prepared in advance. The prepared solution was then transferred

into a Teflon-lined autoclave. The porous carbon aerogels were immersed into the reaction solution. Then the autoclave was heated to at 90 °C and kept for 8 h. The sample was collected and washed thoroughly with deionized water, and dried at 55 °C for 12 h, affording MnCo<sub>2</sub>O<sub>4.5</sub> nanoneedles/carbon aerogel precursor. The precursor was then calcinated at 600 °C for 5 h in N<sub>2</sub> atmosphere and the product was labeled as GMC2. The composites prepared with the cation concentration of half and double that in GMC2 were labeled as GMC1 and GMC3, respectively. The synthetic procedure of pure MnCo<sub>2</sub>O<sub>4.5</sub> nanoneedles was similar to GMC2 without the addition of carbon aerogel. The panoramic schematic route is depicted in Scheme 1.



Scheme 1. The formation mechanism of MnCo<sub>2</sub>O<sub>4.5</sub>/carbon aerogel composites

### 2.3 Structural Characterization

Thermal gravity analysis (TGA) curves of the samples were obtained by a TA Instruments TGA Q5000 equipment in air atmosphere, with heating rate of 5 °C/min. The X-ray powder diffraction (XRD) patterns of the samples were recorded on a Bruker D8 Advance powder X-ray diffractometer with Cu K alpha (use the Greek character) radiation ( $k = 0.15406$  nm) over a 2 h scan range of 20–80°. A Hitachi SU8010A field-emission scanning electron microscope (FE-SEM) was used to characterize the morphology of the composites. High-resolution transmission electron microscopic (HRTEM) images were obtained with a JEOL JEM2100F microscope. Raman spectra were acquired with a Horiba Jobin–Yvon HR 800 spectrometer. The porous characteristics of the porous carbon aerogels were obtained by N<sub>2</sub> adsorption/desorption experiments at 77 K using ASAP 2020 V3.02 H. The specific surface area was measured according to the Brunauer-Emmett-Teller (BET) method.

### 2.4 Electrochemical measurements

To obtain the electrochemical properties of the samples, both the three-electrode and two-electrode configurations were used. According to the conventional optimization methods, the working electrode used in the three-electrode set-up was prepared by casting a Nafion-impregnated sample onto a glassy carbon electrode.<sup>36</sup> Typically, 100 mg of the active material was dispersed in 1 mL of ethanol solution containing 50 µL of Nafion solution (5 wt% in water) by magnetic stirring for 24 h and ultrasonication for 0.2 h. The concentration of the active material in the suspension is 100 mg ml<sup>-1</sup>. The bare glass carbon electrode was polished to a mirror-like surface with 0.3 and 0.05 µm alumina slurry, respectively. The glass carbon electrode surface was cast with 5 µL active material suspension and then dried in the atmosphere. The mass of the active carbon on the glass

carbon electrode is 0.5 mg. A Pt wire and a Ag/AgCl (saturated with KCl (aq)) were used as the counter electrode and the reference electrode, respectively, and an aqueous solution of 2 M KOH was used as the electrolyte. Two-electrode set-up was built in a stainless cell with a glassy fibrous paper as separator and carbon fiber papers as current collectors. The working electrode was fabricated by physically mixing the as-prepared samples and PTFE solution with a weight ratio of carbon to PTFE of 9:1. After stirring for 24 h and milling for 30 min, the mixture was rolled into a slice and then cut to a circular shape with a diameter of 6 mm, and the prepared electrodes were dried at 55 °C overnight to remove deionized water. The mass of each electrode in a symmetric supercapacitor is equal. 2 M KOH, 1M H<sub>2</sub>SO<sub>4</sub> and 1 M Na<sub>2</sub>SO<sub>4</sub> solution were used as aqueous electrolytes.

Cyclic voltammetric (CV), galvanostatic charging/discharging measurements (GCD) and electrochemical impedance spectroscopy (EIS) were performed with a Versastat 2-channel system (Princeton Applied Research). The specific capacitance was calculated from CV curves collected from three electrodes testing according to the equation  $C = \int Idt / mV$ , where  $I$  is the current,  $V$  is the working voltage window, and  $m$  is the mass of the working electrode active material. The specific capacitance from galvanostatic charging/discharging curves was calculated via  $C = It / mV$ . Where  $I$  is the discharge current,  $t$  is the discharge time,  $V$  is the working voltage window, and  $m$  is the mass of the active material at each electrode. The specific capacitance derived from the CV curve and galvanostatic testing through two electrodes testing was determined via  $C = 4 \int Idt / mV$  and  $C = 4It / mV$ , respectively, where  $M$  is the total mass of the active material at the two electrodes. The energy density ( $E$ ) and the power density ( $P$ ) were calculated from galvanostatic charge/discharge testing via  $E = (CV^2) / 2$  and  $P = E / t$ , respectively. Where  $C$  is the specific capacitance from the two electrodes testing and  $t$  is the discharge time.

## 3. Results and Discussion

In order to determine the mass ratio of MnCo<sub>2</sub>O<sub>4.5</sub> to carbon aerogel in GMC1, GMC2 and GMC3, TG analysis was conducted in air atmosphere. The obtained thermal weight loss graph is shown in Fig. S1. For comparison, the TGA results for pure MnCo<sub>2</sub>O<sub>4.5</sub> and carbon aerogel are also displayed in the spectra. Obviously, there is no weight loss for pure MnCo<sub>2</sub>O<sub>4.5</sub>, while the weight loss of pure carbon aerogel is calculated to be 96.3% due to the combustion of carbon. For the composite samples, as shown in Fig. S1, TGA curves have two main weight loss steps up to 500 °C. The first step occurs between room temperature and 100 °C with a weight loss of about 10%, indicating the removal of adsorbed water. The second step with the weight loss of 40–90% occurs between 300 °C to 500 °C, indicating the carbon combustion. The total weight loss of GMC1, GMC2 and GMC3 is about 10.4, 21.7 and 44.2%, respectively. Therefore, the mass ratio of MnCo<sub>2</sub>O<sub>4.5</sub> to carbon aerogel (MnCo<sub>2</sub>O<sub>4.5</sub>: Carbon) in GMC1, GMC2 and GMC3 is estimated to be 1:8, 1:3.3 and 1:1.2, respectively.

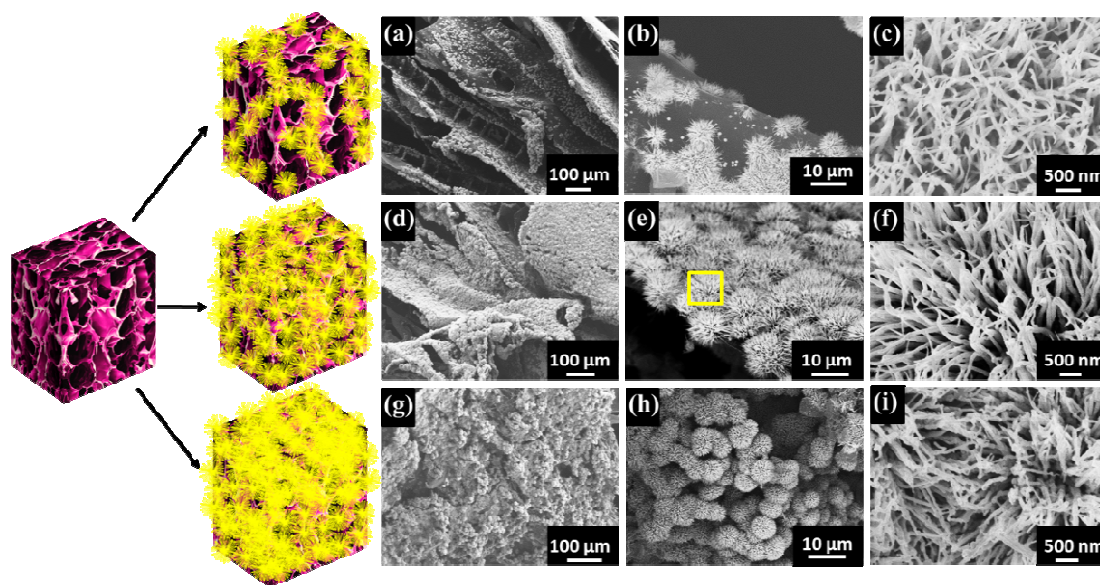


Fig. 1 Representative SEM images of  $\text{MnCo}_2\text{O}_{4.5}$ /carbon aerogel hybrid nanostructures: (a-c) GMC1, (d-f) GMC2, (g-i) GMC3. Images on the left of (a), (d), (e) are the corresponding schematic drawings.

Microstructure of the hybrid nanostructure was characterized by SEM. Fig.1 shows SEM images of the hybrid nanostructures with different mass ratios of  $\text{MnCo}_2\text{O}_{4.5}$  to carbon aerogel. For comparison, the microstructures of the pure carbon aerogel and  $\text{MnCo}_2\text{O}_{4.5}$  precursor were also observed by SEM (Fig.S2). The carbon aerogel exhibits a squashed 3D porous structure with interconnected carbon nanosheets of uniform thickness oriented along a certain direction with the pore size of 30~150  $\mu\text{m}$  (Fig.S2a and b). The low-magnification SEM image of the precursor of  $\text{MnCo}_2\text{O}_{4.5}$  in Fig.S2c reveals the uniform urchin-like hierarchical structures with an average mean diameter of 4~6  $\mu\text{m}$ . In fact, as shown in Fig.S2d, the urchin-like architectures are composed of 1D nanoneedles which are grown radially with a diameter of 30~40 nm and a length of 2~3  $\mu\text{m}$ . After a chemical precipitation process and following the calcination process,  $\text{MnCo}_2\text{O}_{4.5}$  nanoneedles are assembled onto the 3D carbon aerogels (Fig.1). For the sample GMC1, there are some urchin-like nanostructures growing on the surface of the wall of the carbon aerogel (Fig 1a and b). As shown in Fig. 1b, the urchin-like nanostructures did not cover the surface completely, which is contributed to the lack of source of  $\text{MnCo}_2\text{O}_{4.5}$  in the reaction system. As seen on Fig.1b, there are some nuclei on the exposed part of the wall of carbon aerogel. From the image with high resolution (Fig.1c), we can see the urchin-like structure is self-assembled by vertical  $\text{MnCo}_2\text{O}_{4.5}$  nanoneedles with a diameter of ~30 nm, the surface of nanoneedles became coarse and crooked due to the high sinter temperature. With an increase in the mass ratio of  $\text{MnCo}_2\text{O}_{4.5}$  to carbon aerogel, the samples show slightly different morphologies. For the sample of GMC2, all the surface of carbon aerogels is covered by  $\text{MnCo}_2\text{O}_{4.5}$  nanoneedle arrays (Fig.1d). Moreover, as shown in Fig.1e, only a single layer of uniform nanoneedle arrays precipitated on the surface without any redundant urchin-like structures. The morphology of urchin-like structure and the size of nanoneedles are similar with that in

GMC1 (Fig.1f). Fig.S3 is the morphology of the cross section of GMC2 before and after ultrasonic irradiation for 0.2 h, we can see there is no difference on the sample before and after ultrasonic irradiation. The bottom of  $\text{MnCo}_2\text{O}_{4.5}$  nanoneedles connects on the carbon surface directly, facilitating the charge transfer between nanoneedle arrays and carbon aerogels. During the hydrothermal process, a large number of hydroxyl groups and carboxyl groups on the surface of carbon aerogels which formed after KOH activation could adsorb metal ions. These adsorbed metal ions can react with other anion ions to form the precursor, and further form the crystal nuclei at the junction of organic functional groups and metal ions, resulting in the directly growth of  $\text{MnCo}_2\text{O}_{4.5}$  nanoneedles on the carbon surface. However, with the further increase in the mass ratio of  $\text{MnCo}_2\text{O}_{4.5}$  to carbon aerogel, the high mass loading of  $\text{MnCo}_2\text{O}_{4.5}$  in GMC3 results in so many  $\text{MnCo}_2\text{O}_{4.5}$  nanoneedle arrays assembled on the surface of the carbon aerogel that the porous structure of carbon aerogel was blocked (Fig.1g). And from Fig.1h, we can see the excessive urchin-like structures not only covered all the surface of carbon aerogels, but also accumulated on the first layer of  $\text{MnCo}_2\text{O}_{4.5}$  nanoneedles. The morphology of nanoneedles shows no obvious difference among the three samples (Fig.1i). Energy-dispersive X-ray spectroscopy (EDS) analysis of GMC2 in the designated square parts confirms that the composite is composed of C, Mn, Co and O elements (Fig. S4).

The XRD patterns of carbon aerogel,  $\text{MnCo}_2\text{O}_{4.5}$ /carbon aerogel hybrid nanostructure (GMC2) and pure  $\text{MnCo}_2\text{O}_{4.5}$  nanoneedles are shown in Fig.2a. The XRD pattern of carbon aerogels displays two broad peaks at 26.6 and 43.5°, corresponding to the graphite basal plane (JCPDS card no. 26-1079). As for the pure  $\text{MnCo}_2\text{O}_{4.5}$  sample, the detected peaks at 31.3°, 36.8°, 44.8°, 59.5° and 65.3° can be assigned to the (220), (311), (400), (511) and (400) planes in the cubic phase of  $\text{MnCo}_2\text{O}_{4.5}$  (JCPDS card no. 32-0297). For GMC2, all the

diffraction peaks can be well indexed to  $\text{MnCo}_2\text{O}_{4.5}$ . Due to the low intensity, the broad peaks of carbon aerogel are shielded by the diffraction signal of  $\text{MnCo}_2\text{O}_{4.5}$ . The broader diffraction peaks of  $\text{MnCo}_2\text{O}_{4.5}$  can be attributed to the reduced grain size of  $\text{MnCo}_2\text{O}_{4.5}$  nanoneedles on the surface of carbon aerogel.<sup>37</sup>

Raman spectroscopic measurements further confirmed the formation of  $\text{MnCo}_2\text{O}_{4.5}$  in the hybrid structure. Carbon aerogels and pure  $\text{MnCo}_2\text{O}_{4.5}$  were measured as references. The Raman spectra of the three samples are shown in Fig.2b. The typical vibrational bands of carbon aerogels can be found at  $1330\text{ cm}^{-1}$  and  $1583\text{ cm}^{-1}$ , corresponding to the D band and the G band, respectively. Generally, the intensity of the D band represents the concentration of disordered carbon in the sample, while the intensity of the G peak indicates the concentration of graphitized carbon.<sup>3</sup> The pure  $\text{MnCo}_2\text{O}_{4.5}$  nanoneedles show three strong peaks at around  $572$ ,  $780$ , and  $1098\text{ cm}^{-1}$ , which are attributed to the intrinsic peaks of  $\text{MnCo}_2\text{O}_{4.5}$ . All the peaks of carbon aerogels and  $\text{MnCo}_2\text{O}_{4.5}$  nanoneedles can be found in the

spectrum of GMC2, indicating the formation of  $\text{MnCo}_2\text{O}_{4.5}$  on the carbon aerogel.

HRTEM characterization was then employed to further investigate the morphology and microstructures of GMC2. As shown in Fig.2c, the TEM image of  $\text{MnCo}_2\text{O}_{4.5}$  nanoneedles shows the configuration of the urchin-like hierarchical structure. The TEM image at high resolution shown in Fig. 2d further verifies that the urchin-like structure is assembled by 1D nanoneedles, which consist of nanoparticles with the diameter of about  $30\text{ nm}$  and the length of  $2\text{ }\mu\text{m}$ , consistent with the SEM results. The detailed structures were highlighted by high-resolution imaging in Fig.2e. The lattice fringes of  $\text{MnCo}_2\text{O}_{4.5}$  nanoneedles can be identified as having a spacing of  $0.245\text{ nm}$ , corresponding to the (311) planes of  $\text{MnCo}_2\text{O}_{4.5}$ , which is consistent with the XRD pattern results. Selected area electron diffraction (SAED) pattern (inset of Fig.2e) indicates that the  $\text{MnCo}_2\text{O}_{4.5}$  nanoneedles are single crystalline (cubic,  $a=b=c=0.808\text{ nm}$ ). EDS mapping analysis of the nanoneedle fragment also confirmed the formation of  $\text{MnCo}_2\text{O}_{4.5}$  (Fig.2f)

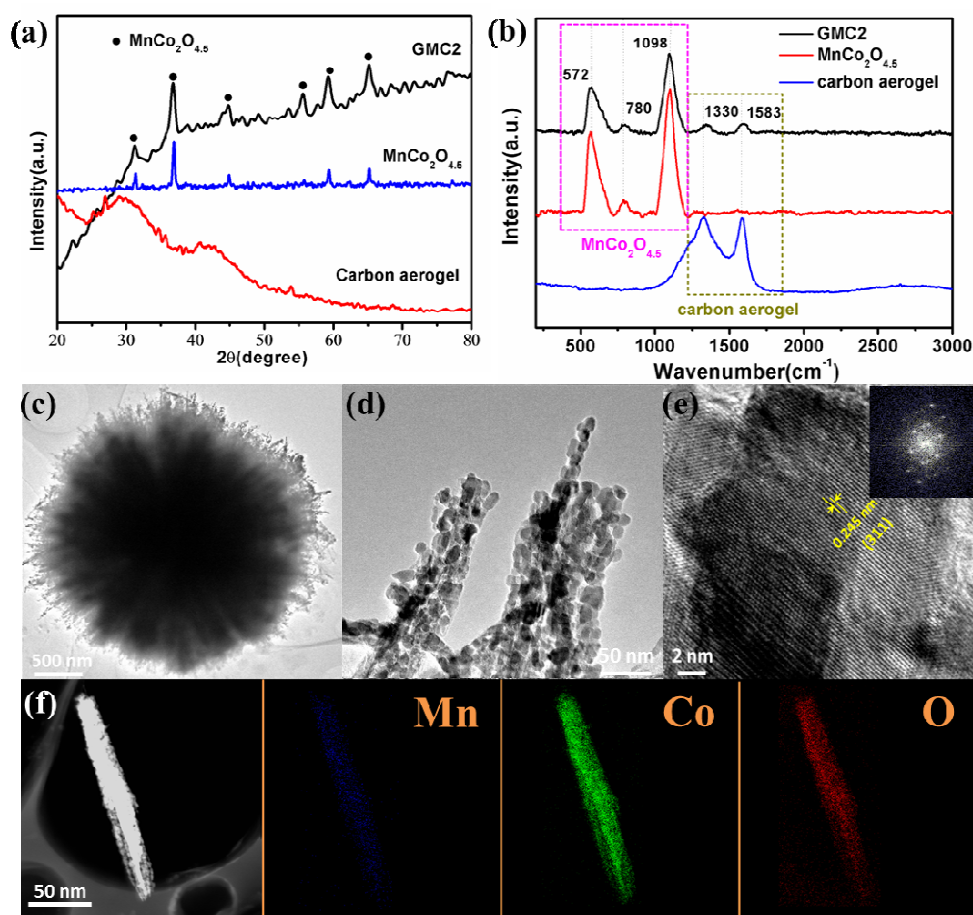


Fig. 2 Structural and morphological characterizations of the samples: (a) XRD patterns and (b) Raman spectra of carbon aerogel, GMC2 and pure  $\text{MnCo}_2\text{O}_{4.5}$  nanoneedles, (c-e) TEM images of GMC2; (f) dark-field TEM image of GMC2 and corresponding EDS mapping of Mn, Co and O. Inset in (e) is the corresponding SAED pattern.

$\text{N}_2$  adsorption/desorption isotherm is used to examine the specific surface area and the pore distribution in the sample. As shown in Fig.3a, GMC2 displays type IV nitrogen adsorption isotherm, indicating different pore sizes from micro- to mesopores. Major adsorption by the samples occurs at a low relative

pressure of less than 0.1, indicating high microporosity in the sample of GMC2. And the rise at 0.5-1.0  $P/P_0$  also proves the existence of mesopores. The specific surface area of GMC2 is about  $888.6\text{ m}^2\text{ g}^{-1}$ , which is much higher than those in metal oxide/carbon aerogel composites ( $\sim 530\text{ m}^2\text{ g}^{-1}$ ).<sup>38,39</sup> Fig.3b is the

differential pore size distribution. GMC2 has both mesopores (2~50 nm) and micropores (< 2 nm). The mesopores have a pore size around 2.73 nm, while the sizes of the micropores are typically centered at 1.27 and 1.59 nm, which are attributing to the KOH activation of carbon aerogels.<sup>35</sup>

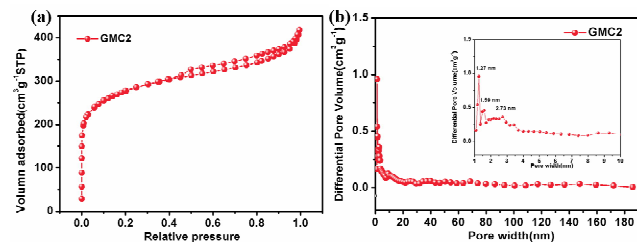


Fig.3 (a) Nitrogen adsorption/desorption isotherm of GMC2, (b) pore size distribution. Inset in (b) is the detail view of (b).

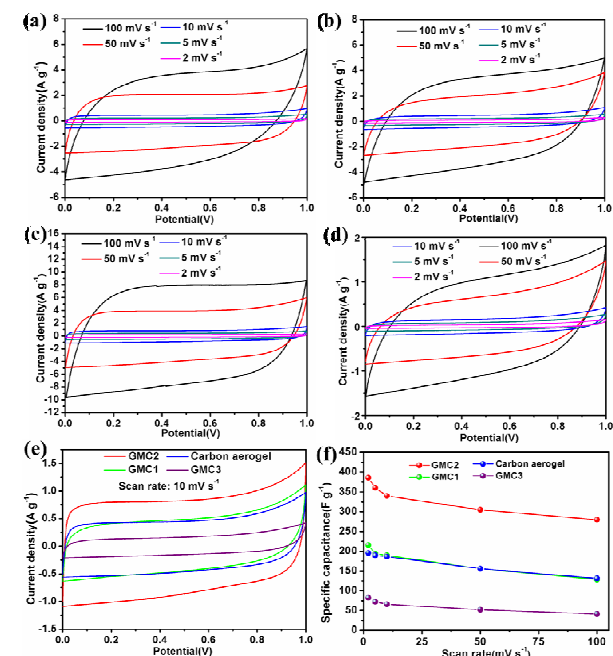


Fig. 4 (a-d) CV curves of the samples at various scan rates in 2 M KOH aqueous electrolyte ((a) carbon aerogel, (b) GMC1, (c) GMC2, (d) GMC3), (e) CV curves of the four electrodes at the scan rate of 10 mV s<sup>-1</sup>, (f) specific capacitance of the four electrodes as a function of scan rate derived from (a-d).

To evaluate the capacitive behavior of the hybrid nanostructures with different mass ratios of MnCo<sub>2</sub>O<sub>4.5</sub> to the carbon aerogel, cyclic voltammetry (CV) tests were carried out using a two-electrode symmetrical set-up in an aqueous electrolyte of 2 M KOH, and the results are shown in Fig.4. The CV scanning tests were performed in the voltage window of 0 to 1 V for all the electrodes at scan rates from 2 to 100 mV s<sup>-1</sup>. As shown in Fig.4a, the carbon aerogel electrode displays nearly rectangular CV curves at all the scan rates, and the charge and discharge part is symmetric, indicating the ideal capacitive performance and high energy storage efficiency. For comparison, the CV profiles of pure MnCo<sub>2</sub>O<sub>4.5</sub> nanoneedles are also displayed in Fig.S5. It is clear that all the curves display Faraday

peaks in the voltage window of -0.1 to 0.5 V at various scan rates in 2 M KOH aqueous electrolyte. When the carbon aerogel is coupled with MnCo<sub>2</sub>O<sub>4.5</sub> nanoneedles, the CV profiles still maintain the rectangular profiles at all the scan rates. From this figure, we can see when MnCo<sub>2</sub>O<sub>4.5</sub> is coupled with carbon aerogel, the current for electrical double layer capacitance overlaps with the current of redox reaction. In this case, the redox peaks still exist since the current density of the hybrid composite from the contribution of both electrical double layer capacitive behaviour and pseudocapacitive behaviour is much higher than that of pure carbon aerogel which only comes from electrical double layer capacitance. For GMC1 electrode, the current density is similar with that of pure carbon aerogel electrode due to the lower loading of MnCo<sub>2</sub>O<sub>4.5</sub> (Fig.4b). As for GMC2 electrode, the CV profiles become more rectangular and the current densities show significant increases compared with those of pure carbon aerogel electrode, suggesting that MnCo<sub>2</sub>O<sub>4.5</sub> can improve the energy storage performance of the carbon aerogel (Fig.4c). Further increasing the loading of MnCo<sub>2</sub>O<sub>4.5</sub> on carbon aerogel, *i.e.* GMC3 electrode and shown in Fig.4d, the CV curves become less rectangular and the current density significantly decreases. Metal oxides usually have poor electrical conductivity. For the GMC3 sample, the mass loading of MnCo<sub>2</sub>O<sub>4.5</sub> is as high as 50%, which can reduce the electrical conductivity of the composite, resulting in the reduced current density. In addition, from SEM images of the samples, it is clear that in the GMC2 sample, the surfaces of the carbon aerogels are fully covered by a single layer of MnCo<sub>2</sub>O<sub>4.5</sub> nanoneedle arrays. The bottom of nanoneedles directly attached to the surface of the wall of carbon aerogel, ensuring high charge transfer speed. When the mass loading of the oxide is lower, as in GMC1, the surface of carbon aerogels cannot be fully covered by the nanoneedles. On the other hand, when the mass loading of MnCo<sub>2</sub>O<sub>4.5</sub> nanoneedles is much higher, as in GMC3, the whole surface of the carbon aerogel is densely covered by MnCo<sub>2</sub>O<sub>4.5</sub> nanoneedles, and there are some urchin-like hierarchical structures loosely adsorbed on the first layer of nanoneedles. Such structure leads to the unsatisfied performance of GMC3 because of the high interface resistance between inorganic nanoneedles. Additionally, the redundant of MnCo<sub>2</sub>O<sub>4.5</sub> nanoneedles can block the porous structure of carbon aerogels. Therefore, for the composite of carbon material and metal oxide, there should be an optimized mass ratio between carbon and metal oxide. In the present study, the best mass ratio of MnCo<sub>2</sub>O<sub>4.5</sub> to carbon aerogel is 1:3.3, as in GMC2. For better observation, the CV curves of the pure carbon electrode, GMC1, GMC2 and GMC3 are shown in Fig. 4e at the scan rate of 10 mV s<sup>-1</sup>. GMC2 displays the highest current density and the largest enclosed area of the CV curves, indicating the enhanced electrochemical performance. The specific capacitance of these four electrodes is calculated from the CV scans and shown in Fig.4f as a function of scan rate. It can be found that the specific capacitance of carbon aerogel is about 195.7 F g<sup>-1</sup> at scan rate of 2 mV s<sup>-1</sup>. With the increasing loading of MnCo<sub>2</sub>O<sub>4.5</sub> nanoneedles, the specific capacitance increases. The specific capacitance of GMC1 and GMC2 is about 215.4 and 385.6 F g<sup>-1</sup> at scan rate of 2 mV s<sup>-1</sup>. However, it can be found that GMC3 has the lowest

specific capacitance, which is about  $82.5 \text{ F g}^{-1}$  at the scan rate of  $2 \text{ mV s}^{-1}$ . Carbon aerogel and GMC1 have similar values at each of the scan rates. Though  $\text{MnCo}_2\text{O}_{4.5}$  can contribute pseudocapacitance to the overall capacitance, it can also reduce the conductivity of the hybrid aerogels. Since the mass loading of  $\text{MnCo}_2\text{O}_{4.5}$  in GMC1 is very little, the positive effect that it provides is offset by the negative influence caused by the reduced conductivity, resulting in the futile modification. GMC2 shows the highest capacitance among all electrodes at the same scan rate, and the specific capacitance at the scan rate of  $2 \text{ mV s}^{-1}$  is almost 2 times higher than that of carbon aerogel. Notably, the specific capacitance value of  $385.6 \text{ F g}^{-1}$  for GMC2 is superior to the reported values for commercial carbon-based electrode ( $\sim 200 \text{ F g}^{-1}$ ),<sup>3, 40</sup> and other metal oxide/carbon-based supercapacitors ( $\sim 350 \text{ F g}^{-1}$ ).<sup>41-43</sup> There are mainly two reasons attributing to the high capacitance. Firstly, the 1D nanoneedle arrays on the surface of carbon aerogels have higher reaction activity than the commonly seen dense composites due to a larger effective surface area. Secondly, taking into account the redox reaction of  $\text{MnCo}_2\text{O}_{4.5}$ , MTMOs can contribute two metal ions to the pseudocapacitance compared with other metal oxides, such as  $\text{MnO}_2$  and  $\text{NiO}$ . For  $\text{MnCo}_2\text{O}_{4.5}$ , there are two electrons involved in the redox reactions of  $\text{Mn}^{2+}/\text{Mn}^{3+}/\text{Mn}^{4+}$  and  $\text{Co}^{2+}/\text{Co}^{3+}$ , contributing to the increased energy storage.<sup>44</sup> Two plausible reactions are described by the following equations.<sup>25</sup>

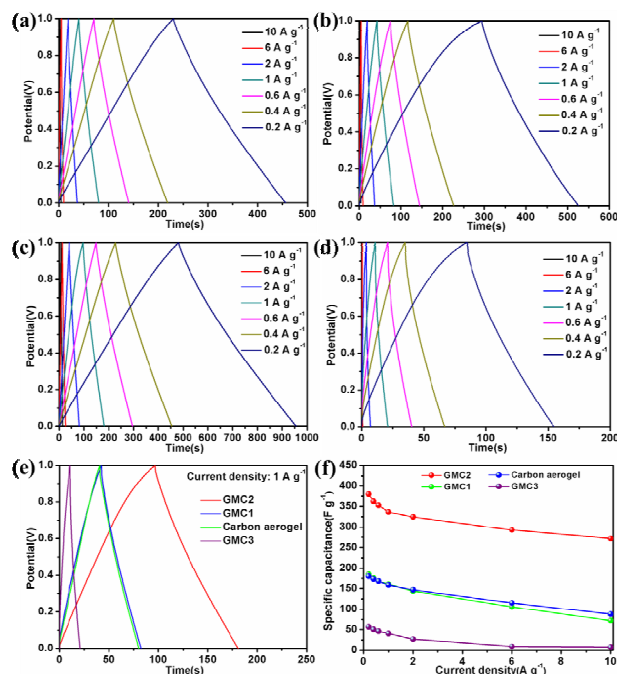
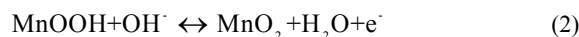


Fig. 5 (a-d) Charge/discharge curves of the samples at various current densities in 2 M KOH aqueous electrolyte ((a) carbon aerogel, (b) GMC1, (c) GMC2, (d) GMC3), (e) charge/discharge curves of the four electrodes at the current density of  $1 \text{ A g}^{-1}$ , (f)

specific capacitance of the four electrodes as a function of current density derived from (a-d).

Fig.5 shows the charge/discharge curves of samples in a voltage range of 0–1 V at different current densities. All four electrodes display nearly isosceles triangular shape with good symmetry at different current densities, indicating high coulombic efficiency (Fig.5a-d). Fig.5e shows the charge/discharge curves of the four electrodes at a current density of  $1 \text{ A g}^{-1}$ . In comparison with other samples, GMC2 exhibits the longest discharge time, confirming the enhanced capacitive behavior. The gravimetric specific capacitance of the samples obtained from the charge/discharge curves is shown in Fig.5f. The sample GMC2 shows the specific capacitance of  $380 \text{ F g}^{-1}$  at the current density of  $0.2 \text{ A g}^{-1}$ , which is much higher than the other three samples.

Electrochemical impedance spectroscopy (EIS) was also conducted on the samples from 0.01 Hz to 100 kHz to compare the electrochemical properties, and the results are shown in Fig.6a. The carbon aerogel shows lower  $Z''$  in the Nyquist plots than hybrid samples.  $\text{MnCo}_2\text{O}_{4.5}$  has poor electrical conductivity and when it is coupled with carbon aerogel, the electrical conductivity of the hybrid composite decreases to be lower than carbon aerogel. The resistance includes two different parts, i.e.,  $Z'$  (the real part of the resistance) and  $Z''$  (the imaginary part of the resistance). The imaginary part  $Z''$  is typically related to the electrical double layer capacitance. In the hybrid composite, the capacitance is originated from both pseudocapacitance and electrical double layer capacitance, but the latter one is less favored due to the cover of the carbon surface by  $\text{MnCo}_2\text{O}_{4.5}$ , leading to the higher  $Z''$  values of hybrid samples. The  $R_s$  value and charge transfer resistance of the electrodes can be derived from the real part of the resistance  $Z'$  in the Nyquist plots. The  $R_s$  resistance can be derived from the intercept of the curve with the horizontal axis and the charge transfer resistance can be determined by the radius of the semi-circle. For an ideal supercapacitor electrode, the  $R_s$  and charge transfer resistance should be as small as possible. We can see that the  $R_s$  gradually increases in the order of carbon aerogel ( $0.59 \Omega$ ), GMC1 ( $0.93 \Omega$ ), GMC2 ( $1.29 \Omega$ ) and GMC3 ( $2.04 \Omega$ ). The increased  $R_s$  for GMC samples can be attributed to the increased loading of  $\text{MnCo}_2\text{O}_{4.5}$  on the carbon aerogel. It should be pointed out that even when the loading of  $\text{MnCo}_2\text{O}_{4.5}$  is as high as 50%, the  $R_s$  for all the GMC samples is still much lower than those metal oxide/carbon composites in literatures.<sup>45, 46</sup> For the charge transfer resistance, the determined value for pure carbon, GMC1, GMC2, GMC3 is about 2.7, 2.08, 1.89 and  $7.96 \Omega$ , respectively. These results are in accordance with the CV data in which the sample GMC2 electrode displays the best supercapacitor performance.

The power densities and energy densities of the symmetric supercapacitors in 2 M KOH aqueous electrolyte are shown in a Ragone plot (Fig. 6b). As shown in Fig.6b, the energy densities of GMC2-based electrode are superior to the values of other samples at the same power density. The energy density can reach as high as  $52.73 \text{ Wh kg}^{-1}$  at a power density of  $0.4 \text{ kW kg}^{-1}$  and  $37.78 \text{ Wh kg}^{-1}$  at a power density of  $20 \text{ kW kg}^{-1}$ , which is about two to ten times higher than the value of the current

supercapacitors ( $5\sim 20\text{ Wh kg}^{-1}$ ).<sup>47-49</sup>

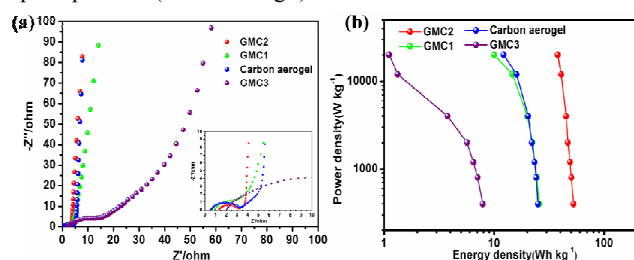


Fig. 6 Nyquist plots and (b) Ragone plots of four electrodes. The image inset in (a) shows the magnified image of the Nyquist plot in high-frequency region showing equivalent series resistance in high frequency region and charge transfer resistance in medium frequency region.

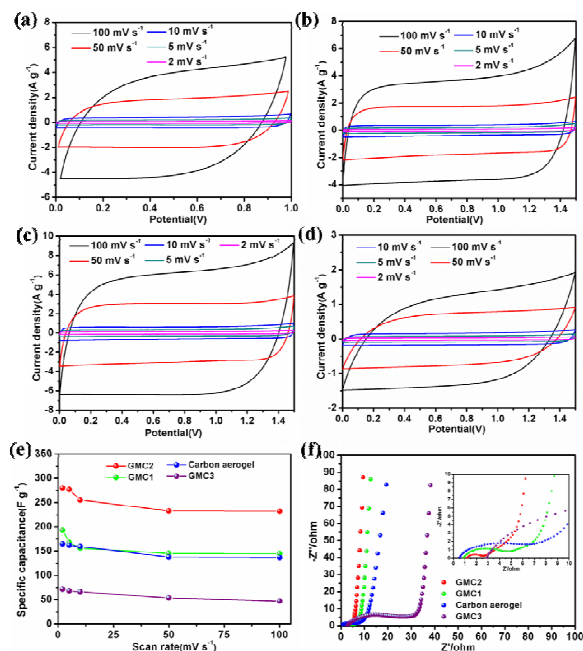


Fig. 7 (a-d) CV curves of the samples at various scan rates in 1 M  $\text{Na}_2\text{SO}_4$  aqueous electrolyte ((a) carbon aerogel, (b) GMC1, (c) GMC2, (d) GMC3), (e) specific capacitance of the four electrodes as a function of scan rate derived from (a-d), (f) Nyquist plots of the four electrodes. The image inset in (f) magnifies the data in high-frequency region showing series resistance in high frequency region and charge transfer resistance in medium frequency region.

Cyclic voltammetry and galvanostatic charge/discharge tests at an extended working voltage were performed for the supercapacitors based different samples. The tests were carried out in 1 M  $\text{Na}_2\text{SO}_4$  aqueous electrolyte, and the results are depicted in Fig. 7. As shown in Fig.7a, the carbon aerogel still maintains a nearly rectangular shape in the voltage window of 0 to 1 V. Fig.7b-7d present the CV curves of the different samples at various scanning rates. Impressively, as shown in Fig.7b-7d, the CV curves of the composite samples exhibit ideal rectangular shapes even in the voltage window of 0 to 1.5 V in 1 M  $\text{Na}_2\text{SO}_4$  aqueous electrolyte and did not reveal any significant increase of anodic current even at 1.5 V. The CV profiles of GMC2 display

nearly mirror symmetry on the inverse voltage even at the scan rate of  $100\text{ mV s}^{-1}$ , indicating excellent reaction reversibility and capacitive behavior. As discussed above, the total specific capacitance of the composites can be divided into two parts, including double layer capacitance provided by carbon aerogels and pseudocapacitance offered by  $\text{MnCo}_2\text{O}_{4.5}$  nanoneedles. In a three-electrode configuration, carbon-based electrodes are known to be working in cathodic range, whereas most metal oxide-based electrodes are known to work well in anodic range. Therefore, the hybrid structure of  $\text{MnCo}_2\text{O}_{4.5}$  nanoneedle/carbon aerogel should have good performance in both anodic and cathodic range. Fig.S6 is the CV curves of the hybrid structure at various scan rates in 1 M  $\text{Na}_2\text{SO}_4$  aqueous electrolyte in the three-electrode set-up. It is clear that all the curves show approximately rectangular CV curves in the voltage window of  $-1$  to  $0.5\text{ V}$  at various scan rates, indicating that the hybrid nanostructure-based electrode presents an ideal supercapacitor behavior. Therefore, it is reasonable that the hybrid nanostructure based electrodes can be charged and discharged in an extended voltage window of  $0$ - $1.5\text{ V}$  in the two-electrode configuration.<sup>50-52</sup> Inset in Fig.S5 is the magnified image of CV curves at the scan rate of  $10$ ,  $5$  and  $2\text{ mV s}^{-1}$ . There is a Faraday peak corresponding to the Faraday redox reaction when the scan rate is slow. However, the CV curve of GMC2 in 2 M KOH aqueous electrolyte at the scan rate of  $100\text{ mV s}^{-1}$  in the two-electrode set-up reveals a significant increase of anodic current at  $1.5\text{ V}$  (Fig.S7). It should be noted that, such a broad voltage window generally cannot be reached in alkaline or acidic electrolytes due to the high polarization of the electrodes in these electrolytes. Fig.7e summarizes the gravimetric specific capacitance of the samples according to the CV test. The GMC3 sample exhibited the lowest specific capacitance of  $71.5\text{ F g}^{-1}$  at  $2\text{ mV s}^{-1}$ . The samples of carbon aerogels and GMC1 displayed an increased specific capacitance of  $164.9$  and  $193.2\text{ F g}^{-1}$  at  $2\text{ mV s}^{-1}$ , respectively. Impressively, the sample of GMC2 showed the highest specific capacitance of  $280\text{ F g}^{-1}$ . Fig.7f shows the Nyquist plots of the four electrodes. As shown in Fig.7f, the  $Z''$  values for all samples exhibit similar values. In  $\text{Na}_2\text{SO}_4$  electrolyte, the electrolyte ions which take part into the electrochemical double layer capacitance are  $\text{Na}^+$  and  $\text{H}^+$ , with smaller radius than that of  $\text{K}^+$ . In addition, the hybrid composites have the same carbon aerogel backbone. Even if the surface of the carbon is covered by  $\text{MnCo}_2\text{O}_{4.5}$  nanoneedles, the smaller  $\text{Na}^+$  and  $\text{H}^+$  are more easier to access to the surface of carbon aerogel than  $\text{K}^+$ . As a result the contribution of electrochemical double layer capacitance in  $\text{Na}_2\text{SO}_4$  electrolyte for these hybrid composites is similar but increased compared to that in KOH solution. Therefore, in the Nyquist plots, the  $Z''$  values for all samples are similar. However, different mass loading of  $\text{MnCo}_2\text{O}_{4.5}$  results in the different pseudocapacitance. Therefore, the samples display different specific capacitance. Additionally, there are significant differences in  $Z'$  values. GMC2 has the smallest charge transfer resistance while GMC3 displays the largest one because of the different mass loading of  $\text{MnCo}_2\text{O}_{4.5}$ , resulting in the different capacitive behaviour of samples.

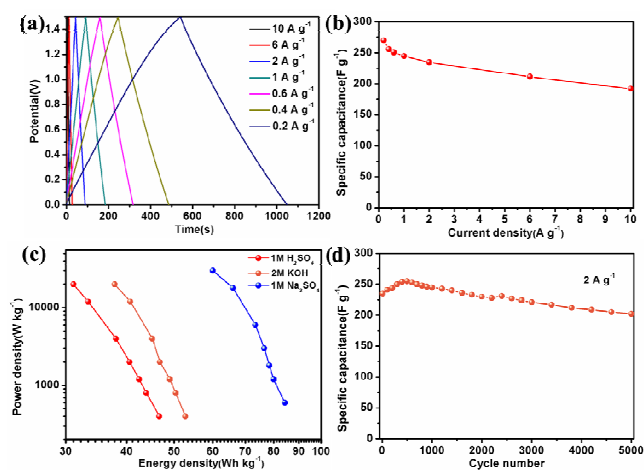


Fig.8 (a) Charge/discharge curves of GMC2 at various current densities in 1 M Na<sub>2</sub>SO<sub>4</sub> aqueous electrolyte, (b) specific capacitance of GMC2 as a function of current density derived from (a), (c) Ragone plots of GMC2 in different electrolytes, (d) cycling performance and capacitance retention at 2 A g<sup>-1</sup> over 5000 cycles.

The galvanostatic charge-discharge curves of GMC2 at various current densities in 1 M Na<sub>2</sub>SO<sub>4</sub> aqueous electrolyte are shown in Fig.8a. All the curves at the operational voltage range from 0 to 1.5 V are nearly isosceles triangles with good symmetry and quick current-voltage response, indicating high coulombic efficiency. The specific capacitances of the electrode were calculated from the discharge curves at different current densities (Fig.8b). The specific capacitance at 0.2 A g<sup>-1</sup> is about 269.9 F g<sup>-1</sup> and still remains at about 192 F g<sup>-1</sup> even at the discharge current density of 10 A g<sup>-1</sup>. The specific capacitance of GMC2 decreases slightly with the increase in the charge/discharge rate, further suggesting good rate capability. Ragone plots of GMC2-based supercapacitor in different electrolytes are shown in Fig.8c. For comparison, the electrochemical properties of GMC2 in acid electrolyte are depicted in Fig.S8. The CV curves of GMC2 in 1 M H<sub>2</sub>SO<sub>4</sub> aqueous electrolyte also display an approximately rectangular shape and the specific capacitance is about 327 F g<sup>-1</sup> at the scan rate of 2 mV s<sup>-1</sup> (Fig.S8a and b). The charge/discharge curves are symmetric at various current densities, as shown in Fig.S8c, indicating a perfect capacitive behavior, and the specific capacitance is about 335.8 F g<sup>-1</sup> at the current density of 0.2 A g<sup>-1</sup> (Fig.S8d). The calculated power densities as well as energy densities in the alkaline, acidic and neutral electrolytes are shown in Fig. 8c. As shown in Fig.8c, the sample of GMC2 in the neutral electrolyte has the highest energy and power density than those in the alkaline and acidic electrolytes due to the extended working potential range (0~1.5 V). The highest energy density is 84.3 Wh kg<sup>-1</sup> obtained at 0.2 A g<sup>-1</sup> with the power density of 600 W kg<sup>-1</sup>. Excellent energy density values of 84.3, 79.9, 78.4, 76.5, 73.3, 66 and 60 Wh kg<sup>-1</sup> were obtained at current density values of 0.2, 0.4, 0.6, 1, 2, 6 and 10 A g<sup>-1</sup>, respectively, corresponding to charge/discharge times of 506, 239.8, 156.8, 91.8, 44, 13.2 and 7.2 s, respectively. These values from the GMC2-based supercapacitor are equivalent to the values of 40~100 Wh kg<sup>-1</sup> for Ni metal hydride batteries,<sup>53, 54</sup> and much higher than the

values of 5~20 Wh kg<sup>-1</sup> for commercial carbon-based supercapacitors,<sup>55, 56</sup> the values of 20~50 Wh kg<sup>-1</sup> for the bimetal compounds-based supercapacitors,<sup>25, 57, 58</sup> and the values of 20~50 Wh kg<sup>-1</sup> of lead-acid cells.<sup>59, 60</sup> In addition, the energy density of the supercapacitors decreases from 84.3 down to 60 Wh kg<sup>-1</sup> with the power density increases from 600 W kg<sup>-1</sup> up to 30 kW kg<sup>-1</sup>, indicating that the energy density of the GMC2-based supercapacitor can be enhanced significantly while maintaining the high power density. The cycle life is one of the most important parameters for the practical application of supercapacitors. The stability test of GMC2-based electrode was conducted under a constant charge and discharge current density of 2 A g<sup>-1</sup> for 5000 cycles (Fig.8d). It is generally accepted that 1D nanostructure grown directly on carbon backbones possesses better mechanical and structural stability compared to powders. The capacitance retention was about 86% with a small decrease from 235 to 202 F g<sup>-1</sup> after 5000 cycles, which is higher than that of many pure metal oxides and metal oxide/carbon hybrid materials.<sup>61, 62</sup> The cycling test at the same operational voltage range, i.e. 1.5 V, did not show any significant capacitance decrease. Additionally, from Fig.8d we can see that the cycling performance first increase and then decrease during the charging/discharging measurements. This is because that when we put the electrode into the electrolyte to test the cycling stability, the electrode cannot be completely wetted at the beginning stage. A small number of electrolyte ions can reach into the interior of the active material. With the increase of cycling number, the electrode was wetted gradually. The number of electrolyte ions involved in the electrochemical reaction increase, further contributing to the enhancement of the capacitance. Until the electrode was wetted completely, we can obtain the highest value of the capacitance. However, continue increasing the cycling number, the capacitance decreased gradually due to the electrochemical stability of the active material.

For our work, although the electrical performance of the hybrid nanostructure is not the best one, the novelty of this work is still apparent because the carbon aerogel and the hybrid material are different with the previous literatures. Firstly, the open study to fabricate the hybrid materials for supercapacitor is mainly based on graphene, carbon nanotube and carbon nanofibers with high cost of manufacturing and raw materials.<sup>1, 7, 62</sup> Few literatures report the utilization of renewable source for the preparation of carbon aerogel to couple with transition metal oxides for supercapacitor applications. More importantly, because of the structure characteristics of chitosan molecules, carbon aerogels derived from chitosan possess high degree of graphitization, good electric conductivity and hierarchical porous structure, which are more competitive than other aerogels as the backbone of hybrid nanostructures. The skeleton of the carbon aerogel is the ideal backbone to support transition metal oxides to increase the energy density. Secondly, mixed transition metal oxides can contribute two metal ions to the pseudocapacitance compared with other metal oxides, such as MnO<sub>2</sub> and NiO. For MnCo<sub>2</sub>O<sub>4,5</sub>, there are two electrons involved in the redox reactions of Mn<sup>2+</sup>/Mn<sub>3+</sub>/Mn<sup>4+</sup> and Co<sup>2+</sup>/Co<sup>3+</sup>, contributing to the increased

energy storage. Additionally, from the morphology of the cross section of GMC2, we can see the bottom of  $\text{MnCo}_2\text{O}_{4.5}$  nanoneedles connects on the carbon surface directly, facilitating the charge transfer between nanoneedle arrays and carbon aerogels. This hybrid nanostructure ensures perfect combination between electrical double layer capacitance and pseudocapacitance. Our study demonstrates the possibility of the preparation of hybrid materials based on renewable source derived carbon aerogel for supercapacitors with high energy density and wide working voltage window. It provides an effective clue to prepare high performance supercapacitor electrode materials with low cost and good sustainability.

#### 4. Conclusions

In summary, we have demonstrated a general route for fabricating hybrid electrodes by assembling metal oxide nanoneedle arrays on the channels of carbon aerogels for high performance electrochemical supercapacitors. The resulting  $\text{MnCo}_2\text{O}_{4.5}$  nanoneedle/carbon aerogels hybrid nanostructure has macro-, meso-, and micro-hierarchical porous structures and possesses an extremely high specific surface area of  $888.6 \text{ m}^2 \text{ g}^{-1}$ . A high stable potential window of 1.5 V for the symmetric supercapacitor was obtained in neutral  $\text{Na}_2\text{SO}_4$  aqueous electrolyte, which is much higher than in KOH or  $\text{H}_2\text{SO}_4$  aqueous electrolytes. Benefiting from the high specific capacitance and broadened working potential range, the energy density reached as high as  $84.3 \text{ Wh kg}^{-1}$  at a power density of  $0.6 \text{ kW kg}^{-1}$  and  $60 \text{ Wh kg}^{-1}$  at a power density of  $30 \text{ kW kg}^{-1}$ .

#### Acknowledgements

The authors are thankful for funding from the National Natural Science Foundation of China (Grant No. 51372142 and 31430031), the Major State Basic Research Development Program of China (No. 2014CB910401), Innovation Research Group (IRG: 51321091) and the "100 Talents Program" of the Chinese Academy of Sciences. Thanks for the support from the "Thousands Talents" program for pioneer researcher and his innovation team, China.

#### Notes

<sup>a</sup> State Key Laboratory of Crystal materials, Shandong University, Jinan 250100, P. R. China. E-mail: hongliu@sdu.edu.cn.

<sup>b</sup> School of Materials Science and Engineering, Georgia Institute of Technology, Atlanta, GA 30032, USA. E-mail: epwong@cuhk.edu.hk  
Electronic Supplementary Information (ESI) available, See DOI: 10.1039/b000000x/

\* Corresponding authors.

#### References

- X. Xia, D. Chao, Z. Fan, C. Guan, X. Cao, H. Zhang, H. J. Fan, *Nano Lett.*, 2014, **14**, 1651-1658.
- Y. Chen, B. Qu, L. Hu, Z. Xu, Q. Li, T. Wang, *Nanoscale*, 2013, **5**, 9812-9820.
- P. Hao, Z. Zhao, J. Tian, H. Li, Y. Sang, G. Yu, H. Cai, H. Liu, C. Wong, A. Umar, *Nanoscale*, 2014, **6**, 12120-12129.
- N. Jha, P. Ramesh, E. Bekyarova, M. E. Itkis, R. C. Haddon, *Adv. Energy Mater.*, 2012, **2**, 438-444.
- J. Yan, Z. Fan, W. Sun, G. Ning, T. Wei, Q. Zhang, R. Zhang, L. Zhi, F. Wei, *Adv. Funct. Mater.*, 2012, **22**, 2632-2641.
- Z. Lei, Z. Liu, H. Wang, X. Sun, L. Lu, X. Zhao, *J. Mater. Chem. A*, 2013, **1**, 2313-2321.
- G. Yu, L. Hu, N. Liu, H. Wang, M. Vosgueritchian, Y. Yang, Y. Cui, Z. Bao, *Nano Lett.*, 2011, **11**, 4438-42.
- B. G. Choi, M. Yang, W. H. Hong, J. W. Choi, Y. S. Huh, *ACS nano* 2012, **6**, 4020-4028.
- P. Sharma, T. Bhatti, *Energy Convers. Manage.*, 2010, **51**, 2901-2912.
- Z. Niu, L. Zhang, L. Liu, B. Zhu, H. Dong, X. Chen, *Adv. Mater.*, 2013, **25**, 4035-4042.
- Z. Niu, H. Dong, B. Zhu, J. Li, H. H. Hng, W. Zhou, X. Chen, S. Xie, *Adv. Mater.*, 2013, **25**, 1058-1064.
- V. T. Le, H. Kim, A. Ghosh, J. Kim, J. Chang, Q. A. Vu, D. T. Pham, J. Lee, S. Kim, Y. H. Lee, *ACS nano*, 2013, **7**, 5940-5947.
- X. Zhao, H. Tian, M. Zhu, K. Tian, J. Wang, F. Kang, R. Outlaw, *J. Power Sources*, 2009, **194**, 1208-1212.
- X. Peng, X. Liu, D. Diamond, K. T. Lau, *Carbon*, 2011, **49**, 3488-3496.
- M. Zhi, C. Xiang, J. Li, M. Li, N. Wu, *Nanoscale*, 2013, **5**, 72-88.
- A. Stein, Z. Wang, M. A. Fierke, *Adv. Mater.*, 2009, **21**, 265-293.
- L. Tongchang, W. Pell, B. Conway, *Electrochim. Acta*, 1997, **42**, 3541-3552.
- C. Hu, K. Chang, M. Lin, Y. Wu, *Nano Lett.*, 2006, **6**, 2690-2695.
- X. Zhao, B. M. Sánchez, P. J. Dobson, P. S. Grant, *Nanoscale*, 2011, **3**, 839-855.
- J. Li, W. Zhao, F. Huang, A. Manivannan, N. Wu, *Nanoscale*, 2011, **3**, 5103-5109.
- C. Hu, J. Chen, K. Chang, *J. Power Sources*, 2013, **221**, 128-133.
- H. Zhou, H. Chen, S. Luo, G. Lu, W. Wei, Y. Kuang, *J. Solid State Electrochem.*, 2005, **9**, 574-580.
- R. Sharma, A. Rastogi, S. Desu, *Electrochem. Commun.*, 2008, **10**, 268-272.
- W. Li, K. Xu, G. Song, X. Zhou, R. Zou, J. Yang, Z. Chen, J. Hu, *CrystEngComm*, 2014, **16**, 2335.
- L. Li, Y. Zhang, X. Liu, S. Shi, X. Zhao, H. Zhang, X. Ge, G. Cai, C. Gu, X. Wang, J. Tu, *Electrochim. Acta*, 2014, **116**, 467-474.
- K. Fic, G. Lota, M. Meller, E. Frackowiak, *Energy Environ. Sci.*, 2012, **5**, 5842.
- M. Galiński, A. Lewandowski, I. Stepniak, *Electrochim. Acta*, 2006, **51**, 5567-5580.
- Y. Chen, X. Zhang, D. Zhang, P. Yu, Y. Ma, *Carbon*, 2011, **49**, 573-580.
- L. Demarconnay, E. Raymundo-Piñero, F. Béguin, *Electrochem. Commun.*, 2010, **12**, 1275-1278.
- X. Du, C. Wang, M. Chen, Y. Jiao, J. Wang, *J. Phys. Chem. C*, 2009, **113**, 2643-2646.
- H. Lee, J. Goodenough, *J. Solid State Chem.*, 1999, **144**, 220-223.
- A. Burke, *J. power sources*, 2000, **91**, 37-50.
- P. Staiti, A. Arenillas, F. Lufrano, J. Menéndez, *J. Power Sources*, 2012, **214**, 137-141.
- Y. Wang, Y. Xia, *Electrochem. Commun.*, 2005, **7**, 1138-1142.
- Pin Hao, Z. Zhao, Y. Leng, J. Tian, Y. Sang, R. I. Boughton, C.P. Wong, H. Liu, B. Yang, *Nano Energy*, 2015, **15**, 9-23.
- L. Mao, K. Zhang, H. S. O. Chan, J. Wu, *J. Mater. Chem.*, 2012, **22**, 80-85.
- S. Mohseni Meybodi, S. Hosseini, M. Rezaee, S. Sadmezhaad, D. Mohammadyani, *Ultrason. Sonochem.*, 2012, **19**, 841-845.
- J. Li, X. Wang, Q. Huang, C. Dai, S. Gamboa, P. Sebastian, *J. Appl. Electrochem.*, 2007, **37**, 1129-1135.
- G. Li, Z. Feng, Y. Ou, D. Wu, R. Fu, Y. Tong, *Langmuir*, 2010, **26**, 2209-13.
- T. Kim, G. Jung, S. Yoo, K. S. Suh, R. S. Ruoff, *ACS nano*, 2013, **7**, 6899-6905.
- J. Li, X. Wang, Q. Huang, S. Gamboa, P. Sebastian, *J. Power Sources*, 2006, **160**, 1501-1505.
- Y. Wu, S. Liu, H. Wang, X. Wang, X. Zhang, G. Jin, *Electrochim. Acta*, 2013, **90**, 210-218.
- Y. J. Lee, J. C. Jung, S. Park, J. G. Seo, S. H. Baek, J. R. Yoon, J. Yi, I. K. Song, *Curr. Appl. Phys.*, 2010, **10**, 947-951.
- H. Wan, J. Jiang, J. Yu, K. Xu, L. Miao, L. Zhang, H. Chen, Y. Ruan, *CrystEngComm*, 2013, **15**, 7649.
- L. Hu, W. Chen, X. Xie, N. Liu, Y. Yang, H. Wu, Y. Yao, M. Pasta, H. Alshareef, Y. Cui, *ACS nano*, 2011, **5**, 8904- 8913.

46. Y. Hu, Y. Zhao, Y. Li, H. Li, H. Shao, L. Qu, *Electrochim. Acta*, 2012, **66**, 279-286.
47. J. Duay, E. Gillette, R. Liu, S. B. Lee, *Phys. Chem. Chem. Phys.*, 2012, **14**, 3329-3337.
48. C. Chen, C. Fan, M. Lee, J. Chang, *J. Mater. Chem.*, 2012, **22**, 7697-7700.
49. L. Peng, X. Peng, B. Liu, C. Wu, Y. Xie, G. Yu, *Nano Lett.*, 2013, **13**, 2151-2157.
50. V. Khomenko, E. Raymundo-Piñero, F. Béguin, *J. Power Sources*, 2010, **195**, 4234-4241.
51. V. Khomenko, E. Raymundo-Pinero, F. Béguin, *J. Power Sources*, 2006, **153**, 183-190.
52. X. Wang, Z. You, D. Ruan, *Chin. J. Chem.*, 2006, **24**, 1126-1132.
53. C. Liu, Z. Yu, D. Neff, A. Zhamu, B. Z. Jang, *Nano Lett.*, 2010, **10**, 4863-8.
54. P. Gifford, J. Adams, D. Corrigan, S. Venkatesan, *J. Power Sources*, 1999, **80**, 157-163.
55. K. An, W. Kim, Y. Park, J. Moon, D. Bae, S. Lim, Y. Lee, Y. Lee, *Adv. Funct. Mater.*, 2001, **11**, 387-392.
56. A. Pandolfo, A. Hollenkamp, *J. power sources*, 2006, **157**, 11-27.
57. L. Shen, J. Wang, G. Xu, H. Li, H. Dou, X. Zhang, *Adv. Energy Mater.*, 2014, 1400977.
58. H. Jiang, J. Ma, C. Li, *Chem. Commun.*, 2012, **48**, 4465-4467.
59. B. Hariprakash, A. Mane, S. Martha, S. Gaffoor, S. Shivashankar, A. Shukla, *Electrochem. Solid-State Lett.*, 2004, **7**, A66-A69.
60. I. Hadjipaschalis, A. Poullikkas, V. Efthimiou, *Renew. Sust. Energ. Rev.*, 2009, **13**, 1513-1522.
61. Y. Wang, Y. Lei, J. Li, L. Gu, H. Yuan, D. Xiao, *ACS Appl. Mater. Interfaces*, 2014, **6**, 6739-6747.
62. X. Dong, X. Wang, J. Wang, H. Song, X. Li, L. Wang, M. B. Chan Park, C. Li, P. Chen, *carbon*, 2012, **50**, 4865-4870.